Distinction of Acoustically Induced Transparency and Autler-Townes Splitting by Helmholtz Resonators

Yi Cheng,[1] Yabin Jin,[2,*] Yukun Zhou,[3] Tong Hao,[3] and Yong Li ⬤[1,†]

[1]*Institute of Acoustics, School of Physics Science and Engineering, Tongji University, 200092 Shanghai, China*
[2]*School of Aerospace Engineering and Applied Mechanics, Tongji University, 200092 Shanghai, China*
[3]*Center for Spatial Information Science and Sustainable Development Applications, Tongji University, 200092 Shanghai, China*

Electromagnetically induced transparency (EIT) and Autler-Townes splitting (ATS) share similar transparent windows in the transmission spectrum, which causes confusion and difficulty in discriminating between them. Essentially, EIT involves asymmetric profile interference, while ATS originates from a strong coupling effect. The conventional method uses the Akaike information criterion (AIC) to calculate the proportion of EIT and ATS, and then determines the dominant phenomenon by experimental data fitting without considering fundamental differences in physics. We present two kinds of acoustic structures by grafting two Helmholtz resonators to a cylindrical tube whose geometrical parameters are chosen by individual mechanisms of acoustically induced transparency (AIT) and ATS. Our results explicitly show AIT and ATS phenomena analytically, numerically, and experimentally, which are also supported by data-fitting and AIC methods. This study contributes to the design of AIT and ATS in their specific applications, avoiding any confusion.

I. INTRODUCTION

A system with three energy levels can generate a variety of interesting phenomena, such as electromagnetically induced transparency (EIT) and Autler-Townes splitting (ATS), which have attracted much attention in the past few decades since ATS and EIT were successively discovered in 1955 [1] and 1990 [2]. EIT originates from ideal phase-out interference between two different stimulated transitions in three-level atomic systems, which leads to a transparent window in the transmittance spectrum [3], with great application prospects for light speed reduction and reduction of group velocity [4–6], among other applications. In acoustics, AIT was also proposed in detuned acoustic resonator and dangling-resonator systems [7–9].

Another phenomenon is ATS, with similar appearance in the spectrum but a different intrinsic mechanism that appears when the frequency of the applied field is tuned to the transition frequency of a given spectral line splitting into several components [1]. ATS is widely studied for three-level spin systems [10], dynamic control of light's frequency and phase [11], high-speed quantum memory and manipulation [12], time-domain gratings [13], and so on. Recently, EIT and ATS were studied in pillared

structures extending to elastic waves for microscale and nanoscale applications [14–17].

This kind of spectral similarity causes much confusion in discerning between EIT and ATS, and much effort has been made to distinguish between them in coupled mechanical-oscillator systems [18], whispering-gallery microcavities [19], three-level atomic systems [20], plasmonic systems [21], metamaterials [22], and so on. Since Anisimov *et al.* [23] first applied the Akaike information criterion (AIC) in three-level atomic systems to distinguish between EIT and ATS from experimental data and determine which plays the main role after calculating their weights [23], the AIC method has been applied to different systems [19,24,25]. However, the AIC is chosen for numerical discernment from experimental data sets without considering the physical principles.

We present a realization of acoustically induced transparency (AIT) and ATS using a pair of Helmholtz resonators (HRs) in air based on their intrinsic mechanisms. Similar acoustic resonators have been studied for Fano-like acoustic transmission [26,27]. By grafting acoustic resonators onto a waveguide, it is feasible to manipulate the transmission with rich physics and analytical expressions, which can be easily fabricated in practice. AIT is designed with Fabry-Perot interference, while ATS is constructed with a strong coupling effect. The spectra of AIT and ATS have one transparent window and two dips, where the

*083623jinyabin@tongji.edu.cn
†yongli@tongji.edu.cn

two dips could be well explained by the surface-response Green's function [28–30]. We fit two models (ATS model and AIT model) to experimental data and get fitting curves intuitively to determine which model works better, and then apply the AIC method to calculate the weight of the two models in a numerical distribution, which proves the effectiveness of our method and shows the complexity of the conventional method. We finally suggest that the isolated AIC method is not sufficient to analyze AIT and ATS, and it needs to consider their fundamental principles to avoid unphysical confusion.

II. ACOUSTICALLY INDUCED TRANSPARENCY

EIT is based on the destructive interference of the transition probability amplitude among three atomic states where a narrow transparent window appears in an originally opaque region and was first observed in optics. Analogously to acoustics, we consider an acoustic system as shown in Figs. 1(a) and 1(c), which consists of two HRs, each with width $L_0 = 12$ mm, height (h_1, h_2) asymmetrically adjusted from 12 mm, center distance L, and two identical necks (radius $r = 4.8$ mm and height $h_0 = 3$ mm) connected to a cylindrical tube with diameter 29 mm to match the inner diameter of the impedance tube. The total length of this structure L_1 is 120 mm. Because of the existence of two HRs, a Fabry-Perot resonant effect will

occur for wavelength $\lambda = 2L/n$ ($n = 1, 2, 3, \ldots$). Therefore, the two HRs and Fabry-Perot resonance act as a three-level system that is able to produce AIT.

We tune the distance L to be 47.9 mm to make the frequency of the Fabry-Perot resonance superposed on that of the HRs. Simulation and experimental methods are both considered as seen in the model and corresponding sample in Figs. 1(a) and 1(c), respectively. The COMSOL MULTI-PHYSICS finite-element method is used for simulation. A plane-wave radiation boundary condition is chosen for the two ends of the tube in Fig. 1(a) and the plane wave is excited at the left end with a frequency range from 2000 to 5000 Hz below the cutoff frequency. Thermal-viscous loss is taken into account in the simulation. The experimental samples made of photosensitive resin are fabricated by three-dimensional printing as shown in Fig. 1(c). The extra length ($d_1 = 20$ mm, $d_2 = 16$ mm) at the two ends acts as a bayonet. The amplitude of the transmission coefficient is measured in an impedance-tube apparatus by the transfer-function method, comprising two Brüel & Kjær type-4206T impedance tubes with the sample sandwiched in between.

The experimental and simulated transmission curves for different pairs of h_1 and h_2 are presented in Fig. 1(b). One can observe that excellent agreement between experiments and simulations is achieved, validating the methods used. In the case of $h_1 = h_2$, one dip exists and no transparent
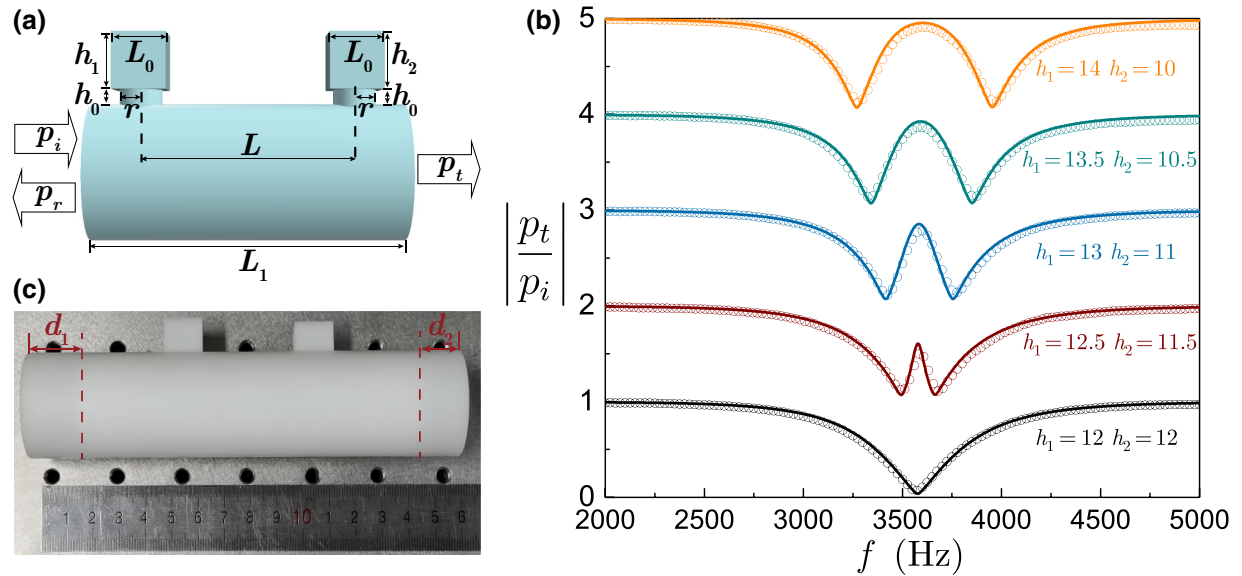

FIG. 1. (a) The HRs for AIT. The sample is hollow, consisting of two rectangular-section cavities of $L_0 \times L_0 \times h_1$ and $L_0 \times L_0 \times h_2$, respectively, and with a cylindrical neck of height h_0 and diameter r. The two HRs are connected to a cylindrical tube of 29-mm diameter at the same side with a distance of L. (b) Experimental data (open circles) and simulation results (solid curves) for the transmission coefficient for five cases. The curves are artificially shifted vertically for clear demonstration. The parameter values are in millimeters. (c) Three-dimensional-printing model of the HRs on the same side. The necks are invisible here because of the model's thickness and their short height. Two additional pipes with lengths d_1 and d_2 are printed for a good seal between the samples and Brüel & Kjær type-4206T impedance tubes.

window appears in the transmission curve because the frequency of the Fabry-Perot resonance coincides with that of the two identical HRs, resulting in a Fabry-Perot bound state in the continuum [16,31]. When the height of the two HRs is antisymmetriclly adjusted while the center distance L is kept fixed, the resonant frequencies of two HRs start to diverge and the effect of the Fabry-Perot resonance becomes observable. Fabry-Perot resonance is stronger with an increase in the difference of h_1 and h_2, so the peak of the transparent window is consequently higher with frequency unchanged after the interference effect. The transmission dip is therefore divided into two individual dips originating from destructive interference between the incident wave and scattered wave by each HR; however, the frequencies of the dips still follow their individual resonant frequencies.

To explain the two dips in the transmission curves with more fundamental insight, we apply a surface-response Green's function [28,29] to the HR system and choose the case of $h_1 = 13$ mm and $h_2 = 11$ mm as an example. The Green's function of a homogeneous one-dimensional system $\overline{G}_{\alpha\beta}$ is related to the heterogeneous surface response $G_{\alpha\beta}$ as

$$G_{\alpha\beta} = \overline{G}_{\alpha\beta}(\overline{Z}, \overline{k}), \tag{1}$$

where $\overline{Z}$ is the effective impedance and $\overline{k}$ is the effective wave number. G_{00} and G_{11} represent monopolar and dipolar modes, which stand for out-of-phase and in-phase displacement of the two surfaces, respectively. G_{01} is a mixed state of monopolar and dipolar modes. G_{00}, G_{11}, and G_{01} can be expressed as

$$G_{00} = \sum_n \frac{\omega^2(\langle p_n(x_0)\rangle + \langle p_n(-x_0)\rangle)^2}{2(\omega_n{}^2 - \omega^2)/B_n},$$

$$G_{11} = \sum_n \frac{\omega^2(\langle p_n(x_0)\rangle - \langle p_n(-x_0)\rangle)^2}{2(\omega_n{}^2 - \omega^2)/B_n}, \tag{2}$$

$$G_{01} = \sum_n \frac{\omega^2(\langle p_n^2(x_0)\rangle - \langle p_n^2(-x_0)\rangle)}{2(\omega_n{}^2 - \omega^2)/B_n},$$

where x_0 and $-x_0$ are the boundary coordinates of the cylindrical tube, the symbol $\langle\rangle$ represents the average value, $\langle p_n(x_0)\rangle$ and $\langle p_n(-x_0)\rangle$ are the surface average boundary pressure, ω_n is the eigenfrequency of the nth mode, and $1/B_n = \int_\Omega p_n^*(x)p_n(x)/B(x)\,dx$, with $B(x)$ being the bulk modulus at position x, $x \in (-x_0, x_0)$. The three heterogeneous surface responses suddenly transit to infinity when the frequency ω is in the vicinity of eigenfrequency ω_n, as shown in Fig. 2(a). The Green's function of a one-dimensional homogeneous system consisting of a
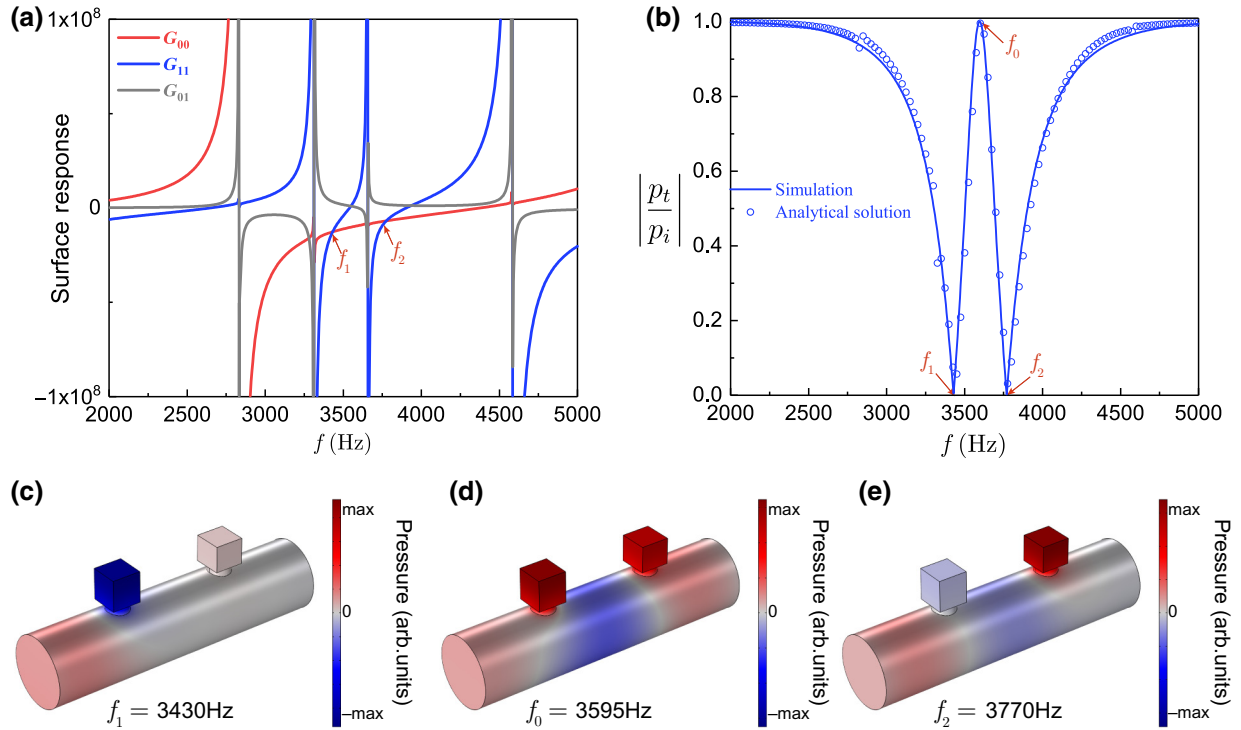

FIG. 2. (a) Three surface responses of the HRs with the effective Green's function with $h_1 = 13$ mm and $h_2 = 11$ mm. (b) Transmission curves from the simulation (open circles) and the Green theorem (solid curve). (c)–(e) Acoustic pressure fields at f_1, f_0, and f_2, respectively. The color bar shows the amplitude of the pressure field.

pair of HRs relates to two effective parameters as follows:

$$\overline{G}_{00} = -\frac{\cot \overline{k}x_0}{\omega \overline{Z}},$$

$$\overline{G}_{11} = \frac{\tan \overline{k}x_0}{\omega \overline{Z}}. \tag{3}$$

Substituting Eqs. (2) and (3) into Eq. (1), we can obtain the effective parameters $\overline{k}$ and $\overline{Z}$ and further deduce the theoretical transmission coefficient $\overline{T}$ of the structure by analogy to the sound wave passing through the middle layer:

$$\overline{k} = \frac{\text{arccot}\left(\sqrt{-\dfrac{G_{00}}{G_{11}}}\right)}{a},$$

$$\overline{Z} = -\frac{G_{00}}{\omega \cot \overline{k}a},$$

$$\overline{T} = \frac{4e^{-i\overline{k}\times 2a}\overline{Z}Z_0}{(\overline{Z}+Z_0)^2 - e^{-i\overline{k}\times 4a}(\overline{Z}-Z_0)^2 - W^2\overline{Z}^2(e^{-i\overline{k}\times 4a}-1)}, \tag{4}$$

where Z_0 is the impedance of air and W is the asymmetry coefficient, which is defined as $W = -G_{01}/[\omega\overline{Z}(G_{11}G_{00} - G_{01}^2)]$. W is 0 when we are dealing with symmetric structures [32,33].

From Fig. 2(b), we can see the predicted transmission coefficient obtained with the effective parameters matches well with the simulation results. Two transmission dips appear at frequencies f_1 and f_2, where $G_{00} = G_{11}$ as contributions of the monopolar mode and the dipolar mode to the surface-response offset result in zero acoustic pressure at the right end of the tube, as shown in the Figs. 2(c) and 2(e). When $G_{00} = G_{11}$, $\overline{k}$ is a pure imaginary value as seen in Eq. (4) so the sound wave cannot propagate to the right end of tube. Figure 2(d) shows the acoustic pressure field at f_0, where the two surface responses are in phase. At f_0, the absolute value of G_{00} is greater than that of G_{11}, so the monopolar mode corresponding to G_{00} accounts for the main contribution to the pressure field. For simplicity, we do not consider the loss effect in Figs. 2 and 4, so the induced transparent window reaches 1 in Fig. 2(b).

III. ACOUSTIC ANALOG OF AUTLER-TOWNES SPLITTING

ATS also has a transparent window with two dips that shows high similarity to the AIT profile in the transmission spectrum but with a different intrinsic mechanism. Since ATS originates from the strong coupling of the two identical HRs, the distance L is required to be much shorter than in the AIT case [16] to avoid a Fabry-Perot effect in the working frequency range. Figures 3(a) and 3(c) show a schematic representation of the structure with two identical HRs at opposite sides of the tube. We change only the center distance L, ranging from 0 to 15.5 mm, with fixed HR height $h_1 = h_2 = 12$ mm; the remaining parameters are the same as in the last section. The extra length ($d_1 = 20$ mm and $d_2 = 16$ mm) at two ends acts as a bayonet. Figure 3(b) shows experimental and simulated transmission curves for different L values. For $L = 0$ mm,
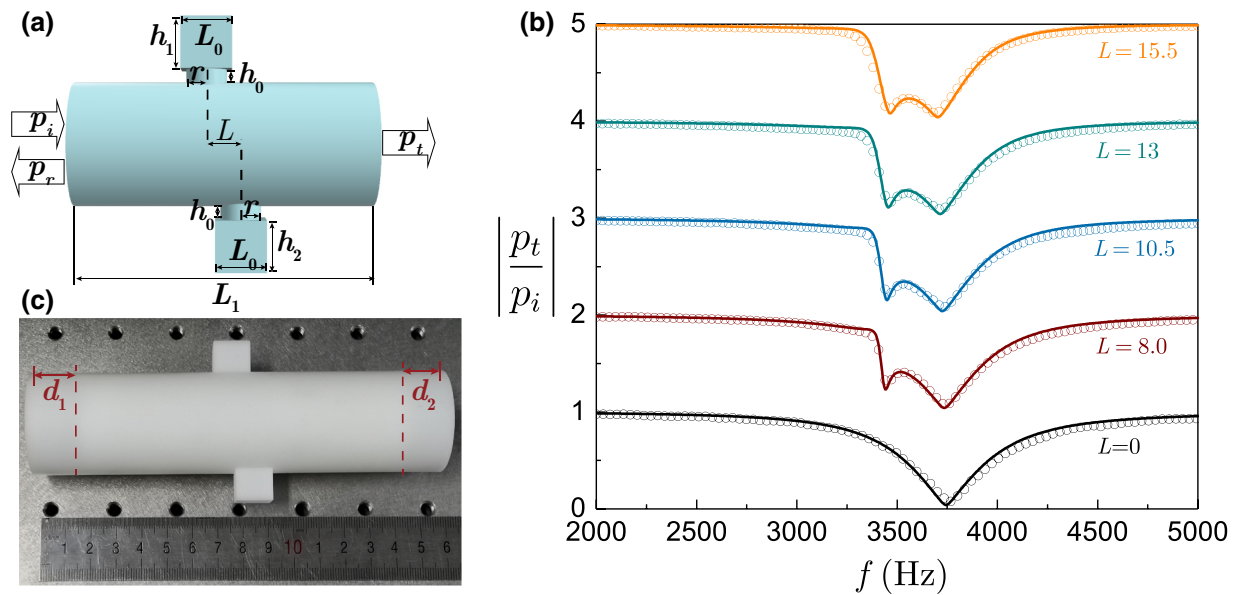

FIG. 3. (a) As Fig. 1(a) but the HRs are placed at the opposite side. (b) Experimental data (open circles) and simulation results (solid curves) for the transmission coefficient in five cases. The parameter values are in millimeters. (c) Three-dimensional-printing model of the HRs on the opposite side.
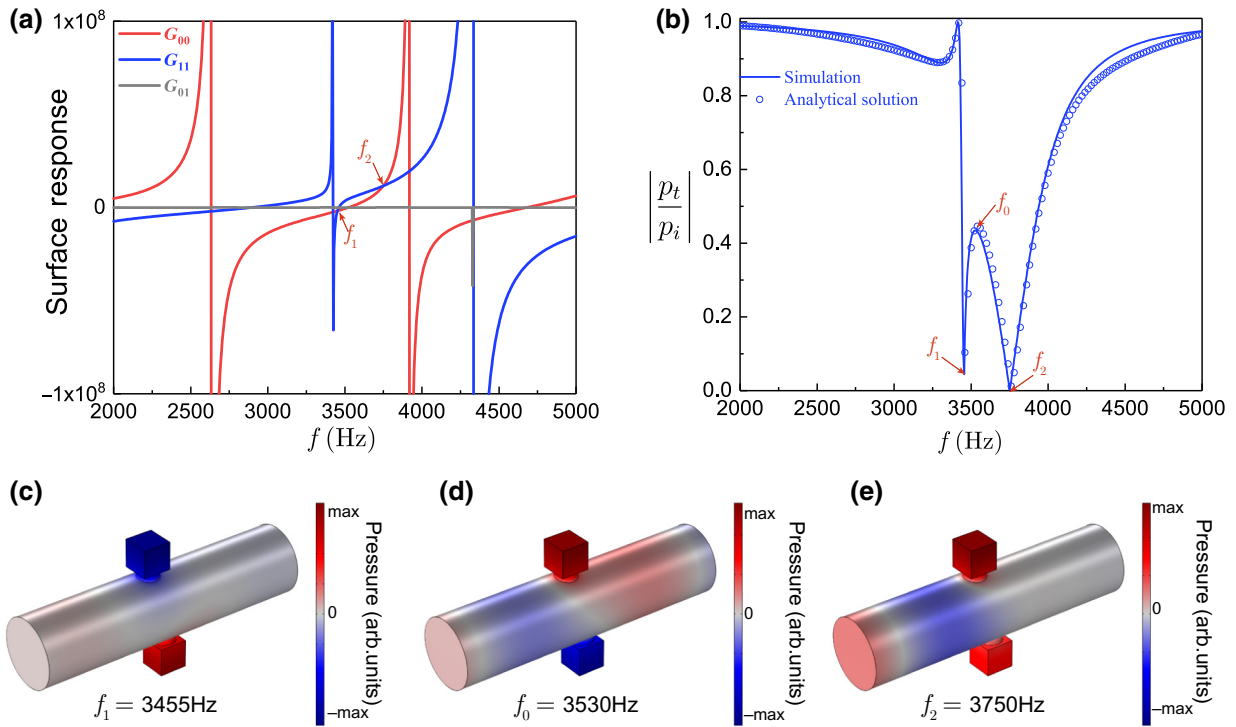
FIG. 4. (a) Three surface responses of HRs for ATS for the case of $L = 8$ mm. (b) Transmission coefficient for simulation (open circles) and the Green theorem (solid curve). (c)–(e) Acoustic pressure fields at three frequencies f_1, f_0, and f_2. The color bar shows the amplitude of the acoustic pressure field.

the two identical HRs are symmetrically grafted to the tube and only one dip occurs in the transmission curve. For $L \neq 0$, the two HRs will couple together and the transmission splits into two dips. In Fig. 3(b), as L increases from 8 to 15.5 mm in steps of 2.5 mm, the coupling between the two HRs becomes weak, so the two dips get close to each other. We choose the case of $L = 8$ mm to explain the ATS mechanism. Similarly, using Eq. (2), we can obtain the heterogeneous surface-response functions G_{00}, G_{11}, and G_{01} as shown in Fig. 4(a). The structure can be regarded as quasisymmetric because the two HRs have identical geometric parameters. Consequently, the off-diagonal term G_{01} of the surface response is much smaller than the diagonal terms G_{00} and G_{11} even at an eigenfrequency that has a small contribution to the surface response. Using Eqs. (3) and (4), we get the theoretical transmission curve without considering loss and compare it with the simulation results as shown in Fig. 4(b), revealing quite good agreement. The two transmission curves split into two dips at frequencies f_1 and f_2, where $G_{00} = G_{11}$ because of the contributions of the monopolar mode and the dipolar mode to the surface response at the right-end offset as shown in Figs. 4(c) and 4(e). $\bar{k}$ is a pure imaginary value at that time sosound waves cannot propagate to the right end of the tube. Figure 4(d) shows the acoustic pressure field at f_0, where the surface responses at the two ends are out of phase since the dipolar mode plays the important role in the surface response. The effect of G_{11} on the curve is greater than that of G_{00} with

the same sign. Consequently, G_{11} has a bigger contribution than G_{00} to the pressure field.

IV. FITTING CURVES TO DISTINGUISH BETWEEN ATS AND AIT

For a given transmission curve with two dips and one transparent window, it is difficult to distinguish between AIT and ATS. Numerical fitting methods [19,20,34] have been proposed to distinguish between ATS and EIT. We can select m points from the transmission curve, and the corresponding coordinates are $(x_0, y_0), \ldots, (x_m, y_m)$, where x_i is the abscissa and y_i is the ordinate $(i = 1, \ldots, m)$. We use the following fitting formulas, which require us to input value $(x_0, \ldots, x_m)$ and compare m obtained values with vertical coordinate values $(y_0, \ldots, y_m)$. The fitting formula for AIT is

$$T_{\text{AIT}} = 1 - \frac{C_+ \left(\frac{\Gamma_+}{2}\right)^2}{(f - f_0 - \varepsilon)^2 + \left(\frac{\Gamma_+}{2}\right)^2} + \frac{C_- \left(\frac{\Gamma_-}{2}\right)^2}{(f - f_0)^2 + \left(\frac{\Gamma_-}{2}\right)^2},$$
(5)

where f_0 is the frequency corresponding to the peak, and $C_+, C_-, \Gamma_+, \Gamma_-$, and ε are free parameters to fit with the experimentally obtained transmission curve. Obviously, the opposite signs of the second term and the third term

cause destructive interference, resulting in a transparent window shown as AIT. The fitting formula for ATS is

$$T_{\text{ATS}} = 1 - \frac{C_1\left(\frac{\Gamma_1}{2}\right)^2}{(f-f_1)^2 + \left(\frac{\Gamma_1}{2}\right)^2} - \frac{C_2\left(\frac{\Gamma_2}{2}\right)^2}{(f-f_2)^2 + \left(\frac{\Gamma_2}{2}\right)^2},$$

(6)

where f_1 and f_2 are the frequencies corresponding to the two dips, and C_1, C_2, Γ_1, and Γ_2 are free parameters to fit with the experimental data. The signs of the second term and the third term are both negative, which is different from the EIT case.

Since the fitting degree is closely related to the selection of the initial value of the free parameter, it is recommended to consider the physical meaning of the free parameter to set a reasonable initial value, where C_1, C_2, C_+, and C_- are the amplitudes of the Lorentzian curves, Γ_1, Γ_2, Γ_+, and Γ_- are their respective full width at half maximum, and ε is the shift from f_0 with a small value. We use the least-squares method to fit the transmission-coefficient equations (5) and (6) with the same experimental data in two cases; the fitting results are shown in Figs. 5(a) and 5(b). As shown in Fig. 5(a), in the case of $h_1 = 12.5$ mm and $h_2 = 11.5$ mm, where the AIT effect appears in Fig. 1(b), the fitting curve using AIT-model Eq. (5) matches very well with the experimental data, the peaks and dips of which are well represented, while the fitting curve obtained with the ATS-model equation (6) absolutely fails to match as expected. The agreement for the AIT model supports the proposed physical mechanism to design acoustically induced transparency with the help of Fabry-Perot resonance. As shown in Fig. 5(b), in the case of $L = 8$ mm, where the ATS effect appears in Fig. 3(b), the ATS model provides a better fitting with the experimental data than the

AIT model for the transparent window, which suggests that the ATS effect originates from the strong coupling between the two HRs without Fabry-Perot resonance.

AIT and ATS are designed with the fundamental physical insights and proved by numerical fitting methods. Here we further apply the AIC to calculate their weights. The AIC is a measure of the relative weight for a test model with a given data set, and estimates the proportion of each model. In the special case of least squares with normally distributed errors, the AIC can be expressed as

$$\mathscr{W}_i^{\text{AIC}} = m \log \hat{\sigma}^2 + 2K_i, \quad i = \text{AIT or ATS},$$

(7)

where $\hat{\sigma}^2 = \left(\sum_{j=1}^{m} \hat{\varepsilon}_j^2\right)/m$, m is the number of values obtained, $\hat{\varepsilon}_j^2$ are the estimated residuals from the fitting model, $\hat{\varepsilon}_j = y_j - \hat{y}$, with y_j being the real value and $\hat{y}$ being the fitting results [35], and K_i is the total number of free parameters in the corresponding model. Thus, the AIC is easy to compute from the results of least-squares estimation. We use the Akaike weight to treat the model as probabilities:

$$W_i = \frac{\exp(-I_i/2)}{\sum_{i=1}^{2} \exp(-I_i/2)}, \quad i = \text{AIT or ATS},$$

(8)

where $I_i = \mathscr{W}_i^{\text{AIC}}/m$.

We plot the AIC weight versus the height difference from Fig. 1(a) in Fig. 6(a) and that of the acoustic structure proposed in Fig. 3(a) as a function of center distance L in Fig. 6(a). Figure 6(a) shows the calculated results for two HRs with different heights ($h_1 \neq h_2$) but fixed distance $L = 47.9$ mm. The per-point weight of the AIT model is greater than 0.5 for 0.4 mm $\leq \Delta h \leq 2.6$ mm, which means AIT pertains. For $\Delta h < 0.4$ mm, Fabry-Perot interference is weak, resulting in a minor peak. For $\Delta h > 2.6$ mm, the frequencies of the two HRs are sufficiently separated and
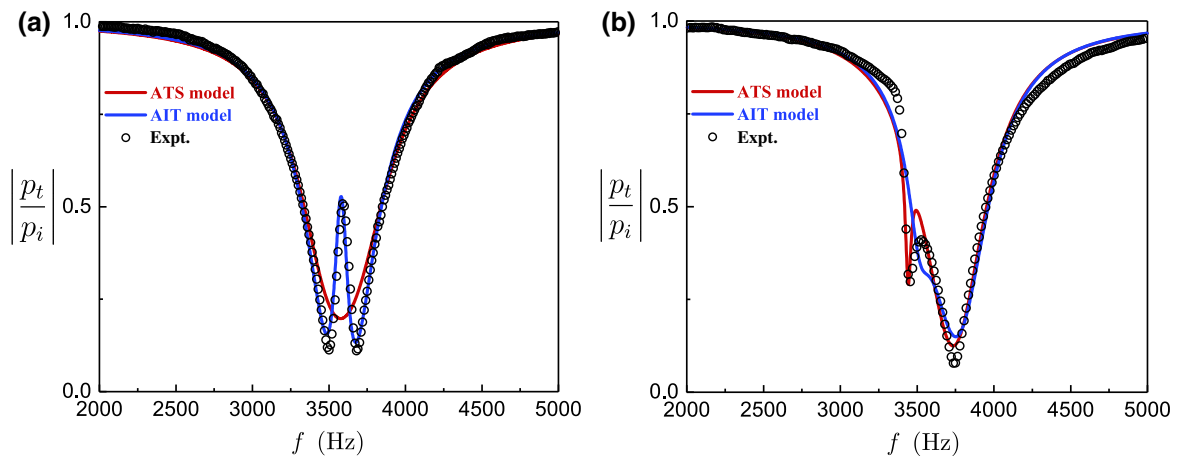

FIG. 5.   Comparison of the fitting curves obtained with the ATS model (red line) and with the AIT model (blue line) with experimental results (open circles) (a) in the case of $h_1 = 12.5$ mm and $h_2 = 11.5$ mm as in Fig. 1(b) and (b) in the case of $L = 8$ mm as in Fig. 3(b).
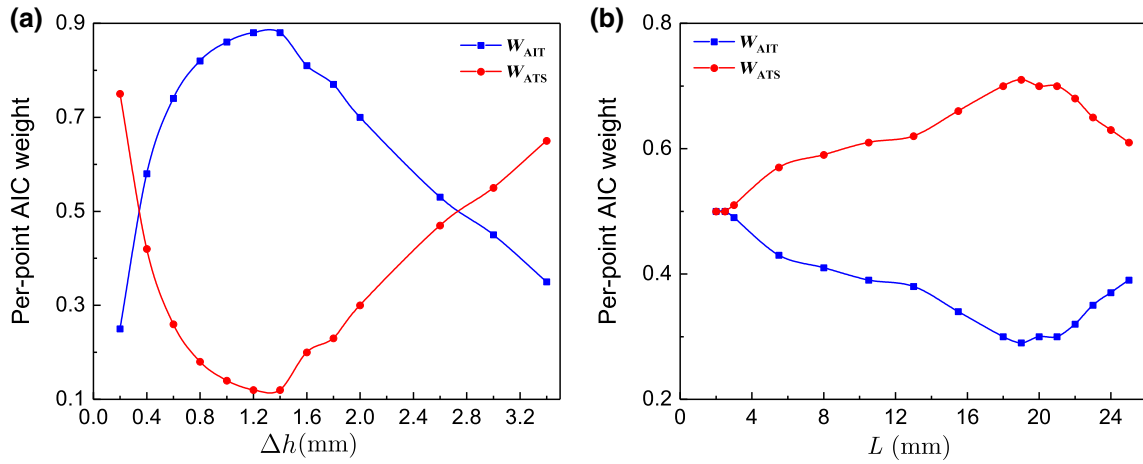
FIG. 6. Per-point AIC weight as a function of (a) height difference ($\Delta h = h_1 - h_2$) and (b) distance L for the acoustic structure presented in Figs. 1(a) and 3(a), respectively, based on simulation data.

so the transmission spectrum behaves like two individual dips with a weak interference effect, as shown by the decrease in W_{AIT}. However, the transmission curve (e.g., $\Delta h > 2.6$ mm) is not induced by the ATS effect as the two dips exactly coincide with their own resonances without a coupling effect, not as W_{AIT} in Fig. 6(a). In Fig. 6(b), the calculation is for two identical HRs, $h_1 = h_2 = 12$ mm. The per-point AIC weight of the ATS model is greater than 0.5 when L is tuned between 3 and 25 mm, so ATS pertains. When $L < 3$ mm, the coupling effect between the two HRs becomes weaker. Although the weights of the EIT model and the ATS model are both 50%, the weight of AIT cannot support the contribution of AIT from the essential physics. From the above, it is important to analyze the AIC weight of AIT and ATS together with their physical principles to avoid any misunderstanding.

V. CONCLUSION

In conclusion, we design two kinds of acoustic structures that generate transparent windows in the transmission spectrum that are shown as AIT and ATS. Each structure has two HRs connected to a cylindrical tube. In the structure where AIT appears, we use two HRs with different heights to obtain different resonant frequencies and select the appropriate value of L to make the Fabry-Perot frequency fall between the resonant frequencies of the two HRs. In the structure in the ATS case, we change L only within small values, eliminating the effects of Fabry-Perot resonance in the frequency range studied to create strong coupling between the two identical HRs and explicitly show the process where an energy level splits in two. Meanwhile, by applying the surface-response Green's function of these two kinds of acoustic structures, we can explain the physical mechanism of the two dips.

Discerning AIT and ATS is complex and lengthy when the AIC method is used. Our designed acoustic structures

depending on AIT and ATS intrinsic mechanisms are able to distinguish them in a simple way while realizing both AIT and ATS in experiments and simulations. The application of the AIC also illustrates that our discerning from the intrinsic mechanism is accurate. However, the AIC method is limited to physically understanding AIT and ATS in a specific parameter domain, which has to take their essential principles into account. Our method can be used for differentiating between AIT and ATS in other three-level systems, and can be designed for potential applications with ensured AIT or ATS. AIT can be applied to design gradient acoustic index structures [36] due to the reduction in sound group velocity; ATS is a good candidate for sensing applications because of the coupling-strength dependence.

[1] S. H. Autler and C. H. Townes, Stark effect in rapidly varying fields, Phys. Rev. **100**, 703 (1955).

[2] S. E. Harris, J. E. Field, and A. Imamoglu, Nonlinear Optical Processes Using Electromagnetically Induced Transparency, Phys. Rev. Lett. **64**, 1107 (1990).

[3] C. Wei and N. B. Manson, Observation of the dynamic stark effect on electromagnetically induced transparency, Phys. Rev. A **60**, 2540 (1999).

[4] L. V. Hau, S. E. Harris, Z. Dutton, and C. H. Behroozi, Light speed reduction to 17 metres per second in an ultra-cold atomic gas, Nature **397,** 594 (1999).

[5] D. Budker, D. F. Kimball, S. M. Rochester, and V. V. Yashchuk, Nonlinear Magneto-optics and Reduced Group Velocity of Light in Atomic Vapor with Slow Ground State Relaxation, Phys. Rev. Lett. **83,** 1767 (1999).

[6] M. M. Kash, V. A. Sautenkov, A. S. Zibrov, L. Hollberg, G. R. Welch, M. D. Lukin, Y. Rostovtsev, E. S. Fry, and M. O. Scully, Ultraslow Group Velocity and Enhanced Nonlinear Optical Effects in a Coherently Driven Hot Atomic gas, Phys. Rev. Lett. **82,** 5229 (1999).

[7] A. Santillán and S. I. Bozhevolnyi, Acoustic transparency and slow sound using detuned acoustic resonators, Phys. Rev. B **84,** 064304 (2011).

[8] A. Santillán and S. I. Bozhevolnyi, Demonstration of slow sound propagation and acoustic transparency with a series of detuned resonators, Phys. Rev. B **89,** 184301 (2014).

[9] E. H. E. Boudouti, T. Mrabti, H. Al-Wahsh, B. Djafari-Rouhani, A. Akjouj, and L. Dobrzynski, Transmission gaps and fano resonances in an acoustic waveguide: Analytical model, J. Phys.: Condens. Matter **20,** 255212 (2008).

[10] S. J. Whiteley, G. Wolfowicz, C. P. Anderson, A. Bourassa, H. Ma, M. Ye, G. Koolstra, K. J. Satzinger, M. V. Holt, F. J. Heremans, A. N. Cleland, D. I. Schuster, G. Galli, and D. D. Awschalom, Spin–phonon interactions in silicon carbide addressed by gaussian acoustics, Nat. Phys. **15,** 490 (2019).

[11] M. Zhang, C. Wang, Y. Hu, A. Shams-Ansari, T. Ren, S. Fan, and M. Lončar, Electronically programmable photonic molecule, Nat. Photon. **13,** 36 (2018).

[12] E. Saglamyurek, T. Hrushevskyi, A. Rastogi, K. Heshami, and L. J. LeBlanc, Coherent storage and manipulation of broadband photons via dynamically controlled Autler–Townes splitting, Nat. Photon. **12,** 774 (2018).

[13] Y. Han, X.-Q. Luo, T.-F. Li, W. Zhang, S.-P. Wang, J. S. Tsai, F. Nori, and J. Q. You, Time-domain Grating with a Periodically Driven Qutrit, Phys. Rev. Appl. **11,** 014053 (2019).

[14] Y. Jin, B. Bonello, R. P. Moiseyenko, Y. Pennec, O. Boyko, and B. Djafari-Rouhani, Pillar-type acoustic metasurface, Phys. Rev. B **96,** 104311 (2017).

[15] Y. Jin, E. I. H. Ei Boudouti, Y. Pennec, and B. Djafari-Rouhani, Tunable Fano resonances of Lamb modes in a pillared metasurface, J. Phys. D: Appl. Phys. **50,** 425304 (2017).

[16] Y. Jin, Y. Pennec, and B. Djafari-Rouhani, Acoustic analogue of electromagnetically induced transparency and Autler–Townes splitting in pillared metasurfaces, J. Phys. D: Appl. Phys. **51,** 494004 (2018).

[17] Y. Liu, A. Talbi, E. H. E. Boudouti, O. B. Matar, P. Pernod, and B. Djafari-Rouhani, Autler–Townes Splitting and Acoustically Induced Transparency Based on Love Waves Interacting with a Pillared Metasurface, Phys. Rev. Appl. **11,** 064066 (2019).

[18] J. Liu, H. Yang, C. Wang, K. Xu, and J. Xiao, Experimental distinction of Autler–Townes splitting from electromagnetically induced transparency using coupled mechanical oscillators system, Sci. Rep. **6,** 19040 (2016).

[19] B. Peng, S. K. Ozdemir, W. Chen, F. Nori, and L. Yang, What is and what is not electromagnetically induced transparency in whispering-gallery microcavities, Nat. Commun. **5,** 5082 (2014).

[20] T. Y. Abi-Salloum, Electromagnetically induced transparency and Autler-Townes splitting: Two similar but distinct phenomena in two categories of three-level atomic systems, Phys. Rev. A **81,** 053836 (2010).

[21] S. X. Xia, X. Zhai, L. L. Wang, B. Sun, J. Q. Liu, and S. C. Wen, Dynamically tunable plasmonically induced transparency in sinusoidally curved and planar graphene layers, Opt. Express **24,** 17886 (2016).

[22] W. B. Lu, J. L. Liu, J. Zhang, J. Wang, and Z. G. Liu, Polarization-independent transparency window induced by complementary graphene metasurfaces, J. Phys. D: Appl. Phys. **50,** 015106 (2017).

[23] P. M. Anisimov, J. P. Dowling, and B. C. Sanders, Objectively Discerning Autler-townes Splitting from Electromagnetically Induced Transparency, Phys. Rev. Lett. **107,** 163604 (2011).

[24] L. Giner, L. Veissier, B. Sparkes, A. S. Sheremet, A. Nicolas, O. S. Mishina, M. Scherman, S. Burks, I. Shomroni, D. V. Kupriyanov, P. K. Lam, E. Giacobino, and J. Laurat, Experimental investigation of the transition between Autler-Townes splitting and electromagnetically-induced-transparency models, Phys. Rev. A **87,** 013823 (2013).

[25] X.-G. Lu, X.-X. Miao, J.-H. Bai, Y. Yuan, L.-A. Wu, P.-M. Fu, R.-Q. Wang, and Z.-C. Zuo, Crossover between electromagnetically induced transparency and Autler–Townes splitting with dispersion, Chin. Phys. B **24,** 094204 (2015).

[26] Y.-F. Wang, V. Laude, and Y.-S. Wang, Coupling of evanescent and propagating guided modes in locally resonant phononic crystals, J. Phys. D: Appl. Phys. **47,** 475502 (2014).

[27] Y.-F. Wang and V. Laude, Longitudinal near-field coupling between acoustic resonators grafted onto a waveguide, Crystals **7,** 323 (2017).

[28] M. Yang, G. Ma, Z. Yang, and P. Sheng, Coupled Membranes with Doubly Negative Mass Density and Bulk Modulus, Phys. Rev. Lett. **110,** 134301 (2013).

[29] M. Yang, G. Ma, Y. Wu, Z. Yang, and P. Sheng, Homogenization scheme for acoustic metamaterials, Phys. Rev. B **89,** 064309 (2014).

[30] Y. K. Zhou, X. S. Fang, D. T. Li, T. Hao, and Y. Li, Acoustic Multiband Double Negativity from Coupled Single-Negative Resonators, Phys. Rev. Appl. **10,** 044006 (2018).

[31] C. W. Hsu, B. Zhen, A. D. Stone, J. D. Joannopoulos, and M. Soljačić, Bound states in the continuum, Nat. Rev. Mater. **1,** 16048 (2016).

[32] M. B. Muhlestein, C. F. Sieck, P. S. Wilson, and M. R. Haberman, Experimental evidence of willis coupling in a one-dimensional effective material element, Nat. Commun. **8,** 15625 (2017).

[33] J. Lau, S. T. Tang, M. Yang, and Z. Yang, Coupled Decorated Membrane Resonators with Large Willis Coupling, Phys. Rev. Appl. **12,** 014032 (2019).

[34] P. Anisimov and O. Kocharovskaya, Decaying-dressed-state analysis of a coherently driven three-level λ system, J. Mod. Opt. **55,** 3159 (2008).

[35] K. P. Burnham and D. R. Anderson, Multimodel inference, Sociol. Methods Res. **33,** 261 (2016).

[36] Y. Jin, B. Djafari-Rouhani, and D. Torrent, Gradient index phononic crystals and metamaterials, Nanophotonics **8,** 685 (2019).